Full length Article

Layered anisotropy within the crust and lithospheric mantle beneath the Sea of Japan

C.P. Legendre [a,b,*], L. Zhao [a], F. Deschamps [a], Q.-F. Chen [c]

[a] Institute of Earth Sciences, Academia Sinica, 128 Academia Road, Sec. 2, Nangang, Taipei 11529, Taiwan
[b] now at Department of Geosciences, National Taiwan University, No. 1, Sec. 4, Roosevelt Rd., Taipei 10617, Taiwan
[c] Key Laboratory of Earth and Planetary Physics, Institute of Geology and Geophysics, Chinese Academy of Sciences, Beijing 100029, China

ABSTRACT

Continental rifting during the Oligocene to mid-Miocene caused the opening of the Sea of Japan and the separation between the Japanese Islands and the Eurasian Plate. The tectonic evolution in the Sea of Japan is important for understanding the evolution of back-arc regions in active convergent margins. Here, we use data from the seismic stations surrounding the Sea of Japan to map the Rayleigh-wave azimuthal anisotropy in the crust and lithospheric mantle beneath the Sea of Japan. We explore the variations of Rayleigh-wave phase-velocity beneath the Sea of Japan in a broad period range (30–80 s). Rayleigh-wave dispersion curves are measured by the two-station technique for a total of 231 interstation paths using vertical-component broad-band waveforms at 22 seismic stations around the Sea of Japan from 1411 global earthquakes. The resulting maps of Rayleigh-wave phase velocity and azimuthal anisotropy allow the examination of azimuthal anisotropy at specific periods. They exhibit several regions with different isotropic and anisotropic patterns: the Japan Basin displays fast velocities at shorter periods (30 and 40 s) with NNE-SSW anisotropy, whereas at 60 s and longer, the velocities become slow even if the anisotropy remains NE-SW; the East China Sea shows fast velocities at all periods (30–80 s) with constant NW-SE anisotropy. Trench-normal anisotropy beneath the Japanese Islands is found at short periods (30–40 s) and become trench-parallel at periods of 60 s and longer. Overall, our model resolves two layers of anisotropy, the shallowest and deepest layers being potentially related to frozen deformation due to recent geodynamic events, and asthenospheric flow, respectively.

© 2016 Elsevier Ltd. All rights reserved.

1. Introduction

The Sea of Japan is a marginal sea of the western Pacific Ocean. It comprises three major basins (Fig. 1): the Japan Basin in the north, the Yamato Basin in the southeast, and the Tsushima Basin (later referred as Ulleung Basin, Yoon et al. (2014)) in the southwest. The thickness of the crust beneath the Sea of Japan changes drastically: the Moho depth is about 22 km beneath the Yamato Rise (Kurashimo et al., 1996), 15 km beneath the Ulleung Basin (Kim et al., 1994), and only 9 km beneath the Japan Basin (Sato et al., 2004). There is a good correlation between the Moho depth and the sea-floor topography, which is widely influenced by the tectonic history of back-arc spreading that formed the Sea of Japan from 32 to 10 Ma (Tamaki, 1992; Pouclet et al., 1994; Choi et al., 2013; Zahirovic et al., 2013, 2014; Yoon et al., 2014). Magnetic

studies (Kobayashi and Isezaki, 1976) and GPS measurements (Takahashi et al., 1999) in this region constrained the regional flow, the location of the transform faulting as well as the spreading centers. In addition, IODP experiments (Tamaki, 1992) and geological investigations (Lallemand and Jolivet, 1986; Takahashi et al., 1999; Yoon et al., 2014) helped constrain the ages of the structures, which were later used to unravel the tectonic evolution of this region (Tapponnier and Molnar, 1976; Fryer, 1996; Yin, 2010). The spreading and dynamic setting of the marginal basins in the western Pacific (Sea of Japan, East China Sea, South China Sea, Philippine Sea, as well as those in southern Pacific) have also been discussed (Miyashiro, 1986; Ren and Li, 2000), as well as the tectonic features (He and Tsukuda, 2003).

The updated plate boundary model of Bird (2003) indicates that the Sea of Japan and its surroundings are complex regions, comprising four small plates (Fig. 1). The Okhotsk plate, associated with the North America plate, includes the northern half of Honshu, Hokkaido, and Shakhalin and is bounded to the east by the Japan subduction zone. The Amur Plate covers most of the Japan
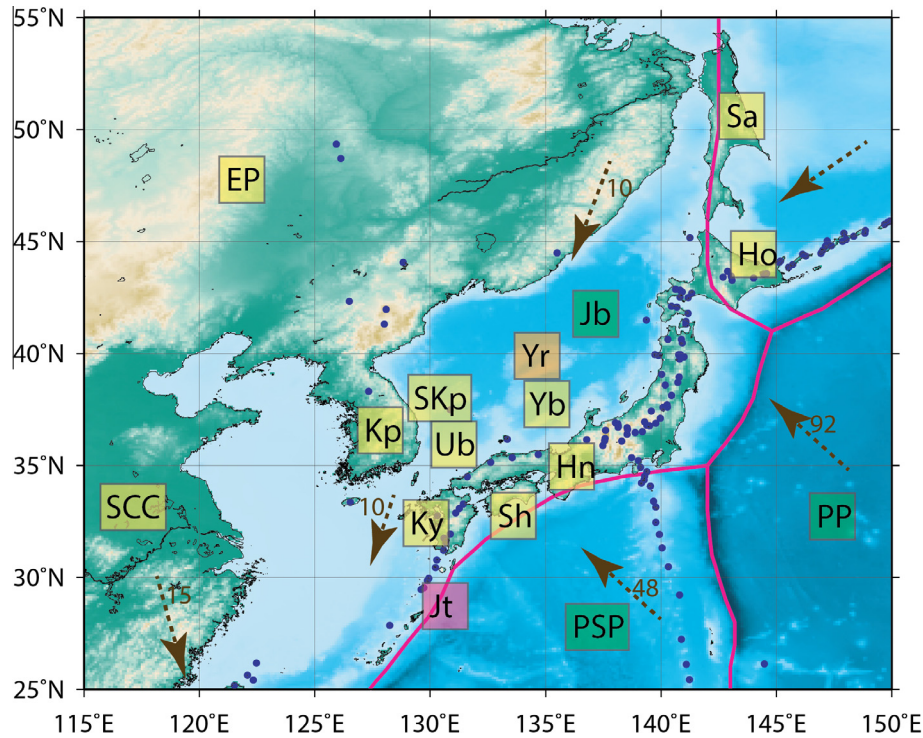
Fig. 1. Tectonic setting of the Sea of Japan. The thick pink lines represent the plate boundaries (Bird, 2003). Blue dots are active volcanoes. Tectonic features include SCC - South China Craton; EP - Eurasian Plate; Jb - Japan Basin; Jt - Japan Trench; Kp - Korean Peninsula; PP - Pacific Plate; PSP - Philippine Sea Plate; Sa - Sakhalin Oblast (Russia); SKp - South Korean Plateau; Ub - Ulleung Basin; Yb - Yamato Basin; Yr - Yamato Ridge. The Japan Peninsula is formed by four main islands: Ho - Hokkaido, Hn - Honshu; Sh - Shikoku; Ky - Kyushu. The yellow boxes indicate the presence of continental crust, whereas the green boxes indicate the presence of oceanic crust. The Absolute Plate Motion (Bird, 2003) is indicated with the brown arrow. (For interpretation of the references to color in this figure legend, the reader is referred to the web version of this article.)

Basin and Korea, and extends northwards. South of Kyushu, the Okinawa plate is bounded to the east by the Ryukyu Arc and covers the eastern part of the East China Sea. Finally, the Yangzte plate extends west of the Okinawa plate and Taiwan. Both the Okinawa and Yangzte plates are associated with the Eurasia plate.

The 3D seismic structure of the Japanese Islands has been investigated extensively. First results by Aki and Kaminuma (1963) and Aki (1968) have been updated later by numerous studies (Hirahara and Mikumo, 1980; Kurashimo et al., 1996; Honda and Nakanishi, 2003; Sato et al., 2004; Matsubara et al., 2005, 2008; Hirose et al., 2008; Bourova et al., 2010; Yoshizawa et al., 2010; Liu et al., 2013; Asamori and Zhao, 2015; Liu and Zhao, 2016). By comparison, the Sea of Japan is less well understood, despite several geological investigations (Lallemand and Jolivet, 1986; Takahashi et al., 1999; Yoon et al., 2014), IODP experiments (Tamaki, 1992; Tobin and Kinoshita, 2006), magnetotelluric studies (Kobayashi and Isezaki, 1976; Pouclet et al., 1994), seismic experiments (Ludwig et al., 1975; Hirata et al., 1989; Kim et al., 1994; Kurashimo et al., 1996; Choi et al., 2012, 2013), noise tomography (Spindel et al., 2003; Zheng et al., 2011), seismic attenuation tomography (Liu and Zhao, 2015), and surface-wave analyses (Abe and Kanamori, 1971; Evans et al., 1978; Sato et al., 2004; Zhao et al., 2011a).

In oceanic regions, where the distribution of seismic stations is uneven and sparse, surface waves play an important role to recover the seismic structure of the lithosphere. Surface-wave analyses can therefore be considered as the best option to resolve the seismic structures beneath the Sea of Japan. Evans et al. (1978) used group speeds of Love and Rayleigh waves to re-examine the original work of Abe and Kanamori (1970), and obtained an average 1D structure along paths north of the Sea of Japan. They showed a lithospheric thickness of about 40 km under the Sea of Japan, which is thinner than typical oceanic lithosphere, and suggested that a simple iso-

tropic model is sufficient to explain the observed dispersion curves of both Love and Rayleigh waves. Aki and Kaminuma (1963) revealed the existence of radial anisotropy in the upper mantle beneath the Japanese Islands from the observation of Love and Rayleigh waves. Aki (1968) then proposed a laminated mantle model to explain the discrepancy between the observed dispersion curves of the Love waves and those estimated from an isotropic shear-wave model.

In the past decade, studies based on acoustic-wave tomography for monitoring the Sea of Japan (Spindel et al., 2003; Lee et al., 2015), body-wave tomography (Hirahara and Mikumo, 1980; Hirata et al., 1989; Zhu et al., 2002; Honda and Nakanishi, 2003; Matsubara et al., 2005, 2008; Hirose et al., 2008; Zheng et al., 2011), surface wave tomography (Friederich, 2003; Huang et al., 2003; Lebedev and Nolet, 2003; Huang and Zhao, 2006; Huang et al., 2009; Legendre et al., 2015b), and other seismic experiments (Choi et al., 2012) provided additional details on the complexity of the structure beneath the Sea of Japan. Recent studies suggested that the formation of the Sea of Japan is related to back-arc extension whereas its evolution is linked to the deep subduction of the Pacific slab as well as the mantle flow induced by the slab subduction (Tatsumi et al., 1990; Lei and Zhao, 2005; Zhao et al., 2009, 2011b; Lei et al., 2011, 2013; Wu et al., 2016). Anisotropic analyses (Montagner and Tanimoto, 1991; Trampert and Woodhouse, 2003) give further constrains on the evolution of the lithosphere beneath the Sea of Japan. The anisotropic pattern at long periods has also been compared with the Absolute Plate Motion of the region (DeMets et al., 1990, 1994).

Azimuthal anisotropy can map the deformation at depth, and may be related to past and present geodynamical events. Surface waves allow for resolving the azimuthal distribution of anisotropic structure (if any) at depth, and may thus be used to reconstruct deformation history of the lithosphere in the study region. Here,

we build maps of isotropic and anisotropic anomalies of the fundamental mode of Rayleigh-wave phase-velocity using teleseismic data from seismic stations around the Sea of Japan. We observe two independent anisotropic layers; the shallower one being associated with the frozen sea-floor spreading anisotropy in the subducting Pacific slab, and the deeper one with current asthenospheric flow.

2. Seismic data and phase-velocity measurements

To measure the Rayleigh-wave phase-velocities beneath the Sea of Japan, we use the waveforms recorded at 22 broadband seismic stations from local and international networks between January 2007 and December 2011. These include 8 stations from the China National Seismic Network (CNSN) (Zheng et al., 2010), one station from the Incorporated Research Institutions for Seismology (IRIS), 10 stations from the National Research Institute for Earth Science and Disaster Prevention in Japan (NIED), and 3 stations from the Korea Meteorological Administration (KMA). Despite a lack of seismic stations in the northern part of the Sea of Japan, the stations we used in this study are almost evenly distributed around our study region (Fig. 2). However, the lack of seismic stations deployed in the Sakhalin Oblast and in the easternmost part of Russia (Fig. 1) limits the coverage in the northeastern part of our study region.

The two-station method, which we use here to measure dispersion curves of Rayleigh-wave phase velocity, was first introduced by Sato (1955) and has been used to measure dispersion curves of surface waves (Knopoff, 1972). In this study, we adopt the implementation of the cross-correlation approach of Meier et al.

(2004) to the two-station method and the inversion scheme of Lebedev et al. (2006) to build anisotropic maps.

The two-station method requires a small angle between the great circle connecting the given two stations and the circle connecting this specific event to the station pair. The station pair and the event are then considered aligned along the same great circle. In this study, we set an upper limit of 10° for this angle. Another condition is that the epicentral distance between the earthquake and the station pair is greater than the distance between the two stations (the epicentral distance must be at least three times larger than the distance between the two stations). This ensures that the difference between the recorded waveforms at the two stations mainly results from the structure between the two stations. In our data set, epicentral distances are between 10° and 170°, and all interstation distances are in the range of 100–2000 km.

Following these criteria, we extracted 26,312 vertical-component sismograms from 1411 selected events (Fig. 3). For each interstation pair, all phase-velocity measurements obtained from earthquakes are averaged to derive the dispersion curve. With 22 stations, the maximum number of station pairs is 231. However, due to differences in the recording times of the selected seismic stations, only 198 could be used. In addition, only high-quality measurements were kept, further decreasing to 168 the total number of interstation paths.

The phase-velocity measurement can be divided into two steps: in the first step, we measure the phase-velocity using broadband regional waveform records to determine the individual interstation dispersion curve for a specific path connecting two stations and for a specific event. For each selected event, the vertical-component
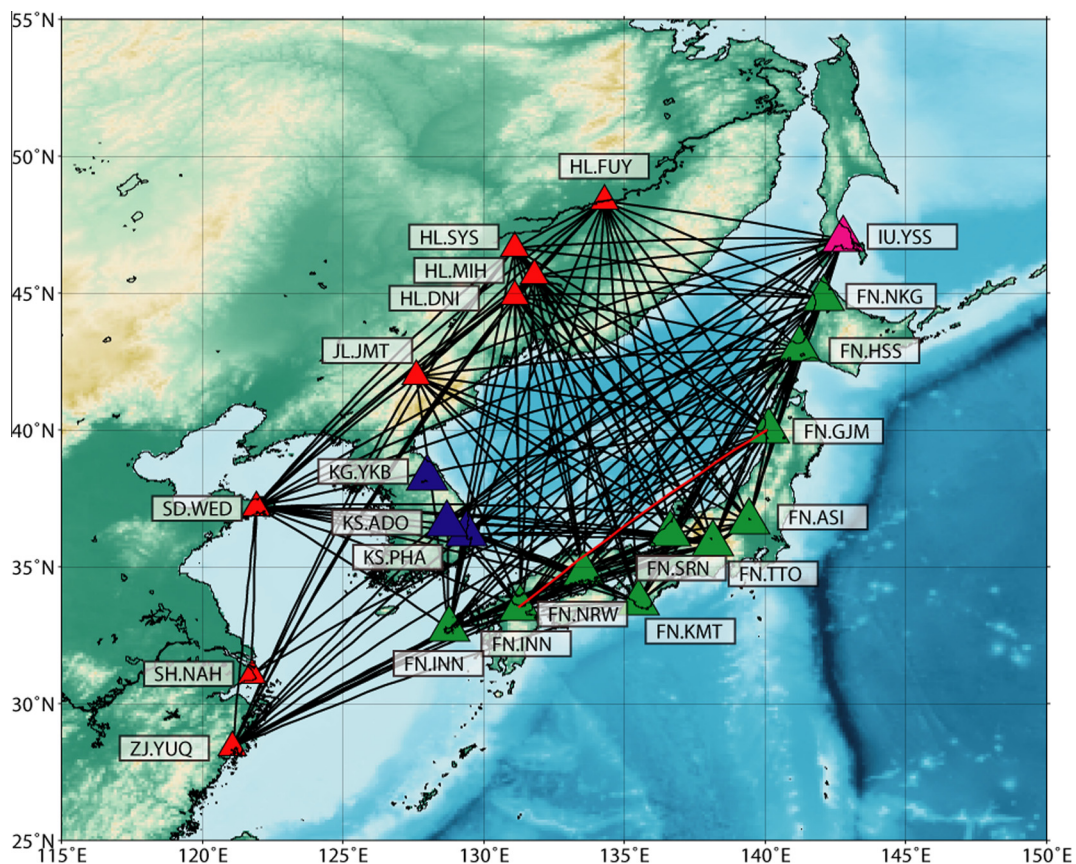
Fig. 2. Stations (triangles) and interstation paths (black lines). The colors of the triangles indicate the network: red (CNSN), blue (KMA), green (FNet) and pink (IRIS). The red path indicates a specific station pair used as an example in Fig. 4 to explain the method. (For interpretation of the references to color in this figure legend, the reader is referred to the web version of this article.)
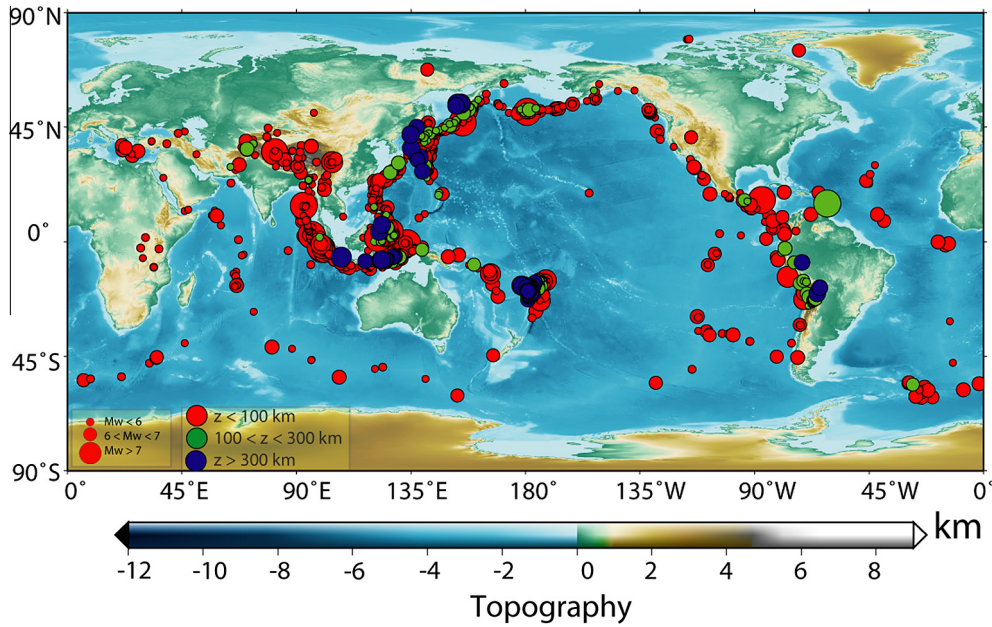
Fig. 3. Seismic events used in this study. They occurred between January 2007 and December 2011. Circles represent the locations of the epicentres, with the colors indicating the depths of the events (red: 0–100 km; green: 100–300 km; blue: 300+ km). The sizes of the circles are proportional to the event magnitudes. (For interpretation of the references to color in this figure legend, the reader is referred to the web version of this article.)

displacements recorded at the two stations in each pair are cross-correlated (Fig. 4).

The cross-correlation function is first filtered with a frequency-dependent Gaussian band-pass filter (Meier et al., 2004) to minimize the effects of noise and interferences. Side lobes caused by interaction of the fundamental mode with scattered waves and higher modes are down-weighted by the application in the time domain of a frequency-dependent Gaussian window to the filtered cross-correlation function. A special effort was made on the quality of the measurements to avoid scattered waves, multi-pathing or off-great-circle propagation which bias our measurements (Legendre et al., 2015c). This approach to filtering and windowing is effective as long as the fundamental mode has the largest amplitude in the seismogram and therefore dominates the contribution to the cross-correlation function (Lebedev et al., 2006; Endrun et al., 2011; Legendre et al., 2012), which is the case of our dataset. The cross-correlation is then transferred to the frequency domain (Fig. 5), and its complex phase is used to calculate the Rayleigh-wave phase-velocity $C(\omega)$, as detailed in previous studies (Meier et al., 2004; Lebedev et al., 2006; Deschamps et al., 2008; Endrun et al., 2011; Legendre et al., 2014a,b, 2015a).

In the second step, for each selected station pair, all measurements from available earthquakes are averaged, resulting in a single path-specific dispersion curve (Fig. 6). Averaged dispersion curves that are constrained by at least 5 single event-specific dispersion curves are kept for further analyses, and the rest are discarded. We repeated this procedure for each station pair, and obtained a collection of 168 phase velocity dispersion curves for the fundamental mode Rayleigh wave (Fig. 7).

As the interstation distance is relatively large (on average, around 1500 km), measurements at short periods (30 s and shorter) are less robust. Because here we focus on the structure of the upper lithospheric mantle beneath the Sea of Japan, which is sampled by periods in the range 20–100 s, this limitation alters only very slightly our results. Our data set allowed measuring dispersion curves between 5 and 300 s, which we then invert for maps of Raleigh-wave velocity anomalies at selected periods between 30 and 80 s, for which we have a good regional and azimuthal coverage (Fig. 8). According to depth-sensitivity kernels (Fig. 9), this range of period samples the whole crust and the lithospheric mantle.

3. Inversion for phase-velocity maps

To recover maps of Rayleigh-wave velocity anomalies, we then invert our collection of dispersion curves for both isotropic and azimuthally anisotropic (2ψ and 4ψ) Rayleigh-wave phase-velocity maps at selected periods. At each point of the model, the total velocity anomaly can be parameterized with 5 coefficients: one for the isotropic phase-velocity variation, δC_{iso}, 2 for the 2ψ-variation, $A_{2\psi}$, and $B_{2\psi}$, and 2 for the 4ψ-variation, $A_{4\psi}$, and $B_{4\psi}$ (Deschamps et al., 2008; Endrun et al., 2011):

$$\delta C = \delta C_{iso} + A_{2\psi}\cos(2\psi) + B_{2\psi}\sin(2\psi) + A_{4\psi}\cos(4\psi) + B_{4\psi} \times \sin(4\psi), \tag{1}$$

where ψ is the local azimuth of the ray. The amplitudes of azimuthal velocity variation (Λ) and the directions of fast propagation (θ) of the 2ψ- and 4ψ-anisotropy are then given by:

$$\begin{cases} \Lambda_{2\psi} = \sqrt{A_{2\psi}^2 + B_{2\psi}^2} \\ \theta_{2\psi} = \frac{1}{2}\arctan\left(\frac{B_{2\psi}}{A_{2\psi}}\right) \end{cases} \text{ and } \begin{cases} \Lambda_{4\psi} = \sqrt{A_{4\psi}^2 + B_{4\psi}^2} \\ \theta_{4\psi} = \frac{1}{4}\arctan\left(\frac{B_{4\psi}}{A_{4\psi}}\right). \end{cases} \tag{2}$$

Note that in Eq. (2), the calculation of the fast directions for 2ψ and 4ψ anisotropy ($\theta_{2\psi}$ and $\theta_{4\psi}$, respectively), takes into account the π-periodicity of the arctangent function.

The model is parameterized on a triangular grid of knots (Wang and Dahlen, 1995) with a grid spacing of 50 km. Each dispersion curve yields the average phase-velocity along the path linking the two stations as a function of period. The total average phase-velocity anomaly along the ith path may be written as the integral of local anomalies at each grid knot sampled by the given path,

$$\overline{\delta C_i} = \int_\varphi \int_\theta K_i(\varphi,\theta)\,\delta C(\varphi,\theta)\,d\theta\,d\varphi, \tag{3}$$
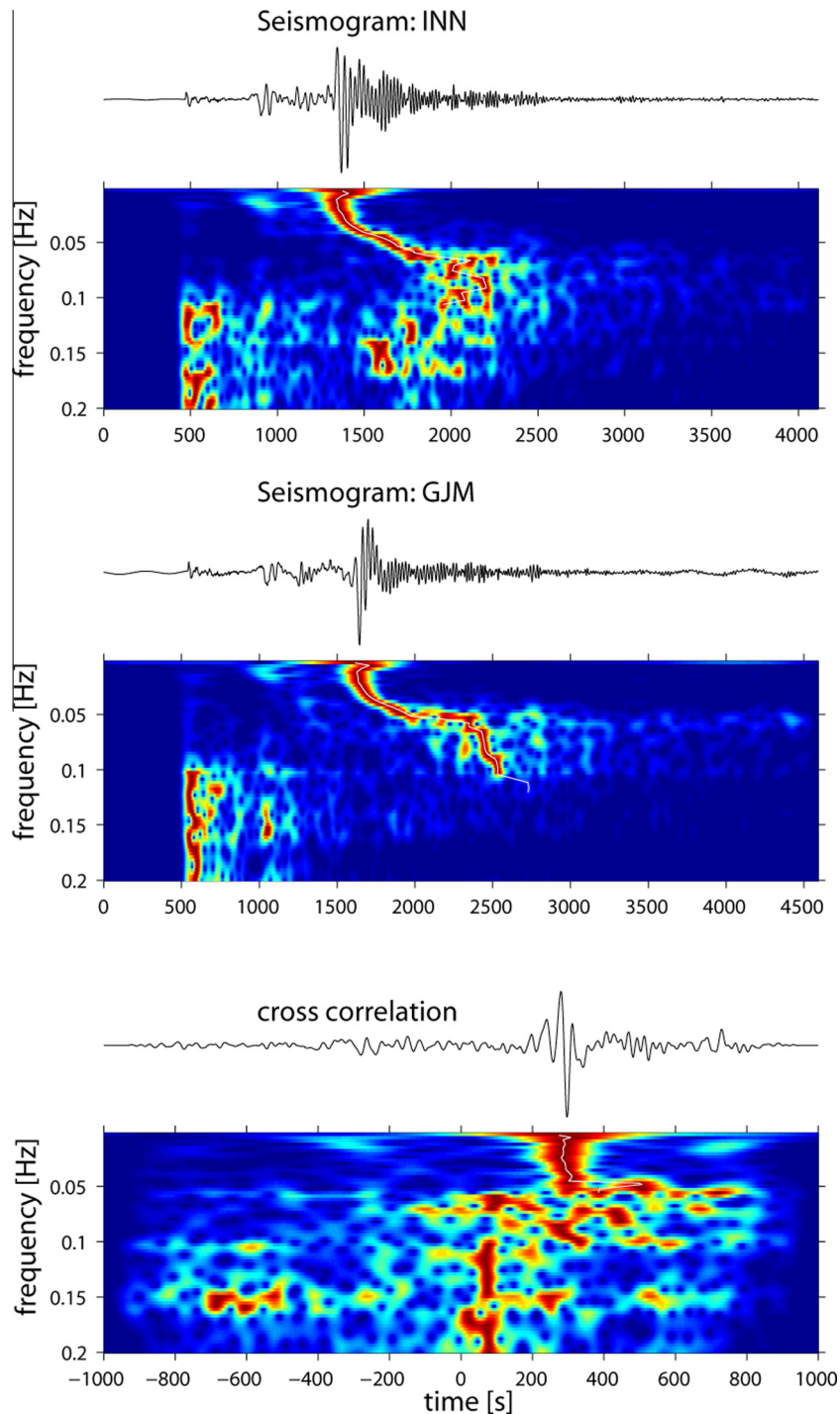
Fig. 4. Vertical components of the displacement recorded at the pair of stations (top and center) and the cross-correlation function (bottom). The color plots show the time–frequency diagram of the energy, where warm colors in the images indicate higher energy, and the maximal energy is plotted with a thin white line. (For interpretation of the references to color in this figure legend, the reader is referred to the web version of this article.)

where the local anomalies $\delta C(\varphi, \theta)$ are weighted by the sensitivity kernels $K_i(\varphi, \theta)$. The kernels provide the contribution at each knot on a specific path to the total phase-velocity anomaly (Lebedev and Van Der Hilst, 2008). The phase-velocities obtained from the dispersion curves are averaged for each period, and the inversion is performed to obtain the phase-velocity perturbations relative to the regional average model.

Previous studies (Montagner and Tanimoto, 1990; Trampert and Woodhouse, 2003) pointed out that the amplitude of 4ψ anisotropy is comparable to that of the 2ψ anisotropy, and should thus be taken into account in the inversion (Eq. (3)).

In our models, we also found that the amplitude of the 2ψ anisotropy (defined in Eq. (2), displayed in Fig. 10) is larger than that of the 4ψ term by a factor of 2, consistent with previous studies using the same techniques (Deschamps et al., 2008; Legendre et al., 2014a,b, 2015a). In our inversions, we consider the phase velocity variation to be in the form of Eq. (1), i.e. isotropic part, 2ψ part and 4ψ part. The inversion results show that these three parts have different amplitudes, with the isotropic part being dominant compared to the anisotropic contributions, and the 2ψ anisotropy being slightly stronger than the 4ψ anisotropy (Fig. 10). We consider all three parts in the
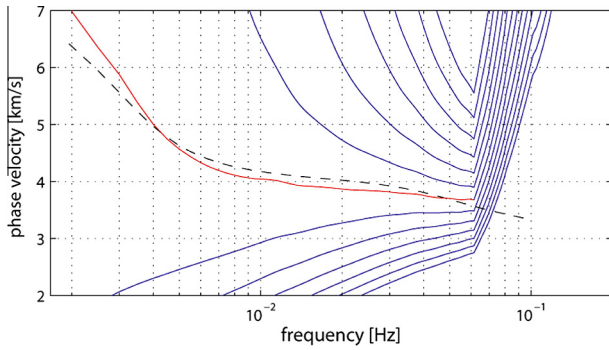
Fig. 5. Inversion of the cross-correlation function for a phase-velocity dispersion curve. Possible solutions are represented by an array of curves (blue lines). The model-predicted phase-velocity for the Rayleigh wave in Earth Model AK135 is displayed in dashed line. The red part of the curve is the dispersion range selected for this specific event. (For interpretation of the references to color in this figure legend, the reader is referred to the web version of this article.)
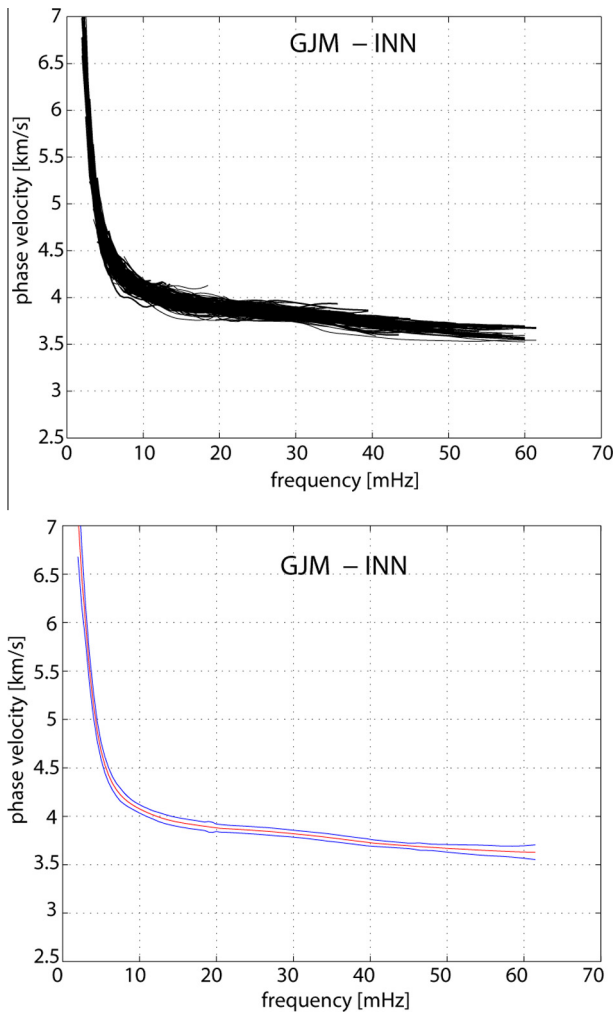
Fig. 6. Individual phase-velocity curves measured for different earthquakes (top) and the average (bottom) with standard deviation (blue lines). (For interpretation of the references to color in this figure legend, the reader is referred to the web version of this article.)
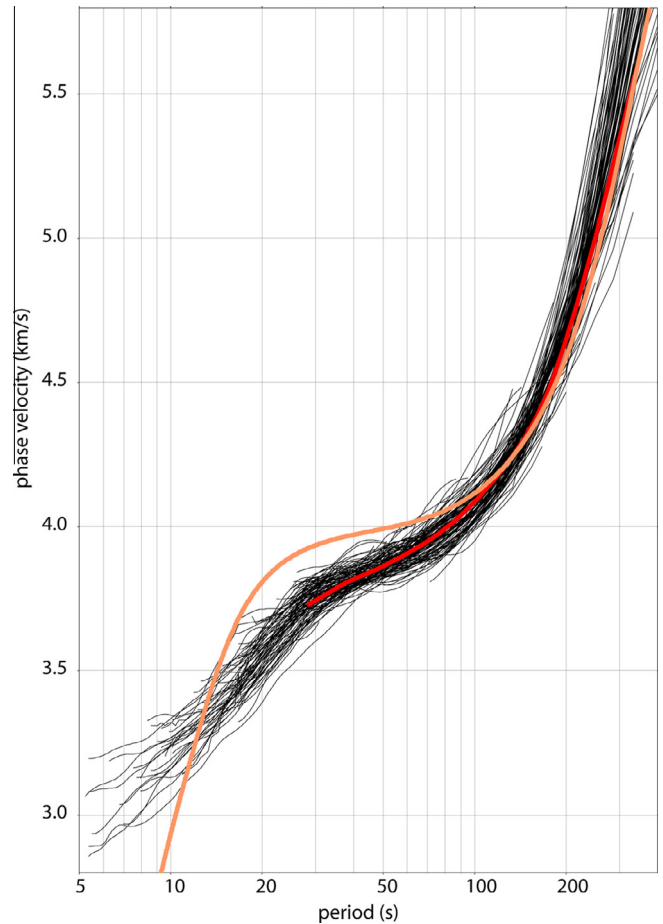

Fig. 7. Manually measured phase-velocity curves (black) for all station pairs. The orange line is the predicted phase-velocity calculated from a 1D reference Earth Model AK135 (Kennett et al., 1995), and the red line is the average curve for the study region. (For interpretation of the references to color in this figure legend, the reader is referred to the web version of this article.)

2ψ anisotropy, which can be related to Lattice Preferred Orientation (LPO) and/or Shape Preferred Orientation (SPO) and to regional deformation, there is no clear mechanism to which 4ψ anisotropy can be linked. Therefore, we do not interpret 4ψ result because it has smaller amplitude than 2ψ part (see discussion on the reduced χ^2 below).

To control the quality of our inversions, we performed a series of tests and corrections. First, we detect and reject the dispersion curves that showed excessive deviations from the average (Legendre et al., 2014a). For this purpose, we calculated the average phase velocity at each period using all the dispersion curves in Fig. 7 and its first and second derivatives. Then, using a simple least-squares misfit function, we rejected a certain amount of our dataset to remove possible errors and inconsistent data, which might affect our final model. Note that we applied this procedure independently for each period. The results of these tests are displayed in Fig. 11 and show that the dataset is very consistent. With only 40% of the dataset (Fig. 11c), the general pattern of the inversions does not change much compared to other models with less data rejection (Fig. 11a and b). For our preferred model, we selected a rejection threshold of 30%. Removing more than 30% of the less consistent dispersion curves did not affect much the resulting model (except the anisotropic pattern). Furthermore, similar structures to those obtained with higher rejection rates may be obtained by increasing the smoothing of the isotropic term.

inversion because 2ψ and 4ψ parts can reduce the residuals. It is important to note that, including 4ψ anisotropy or not doesn't change the isotropic and 2ψ anisotropy models. However, unlike
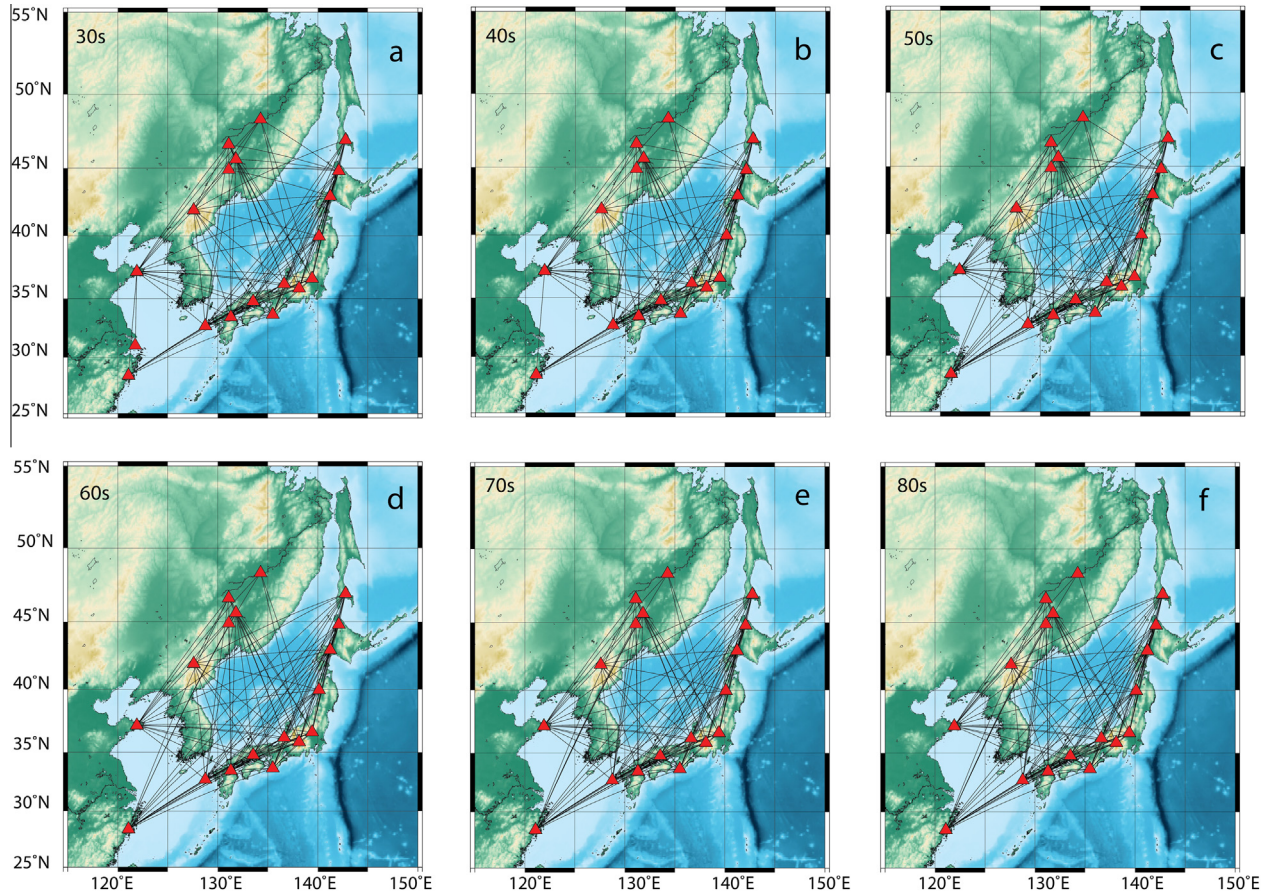
Fig. 8. Inter-station paths that provide phase-velocity measurements at specific periods: (a) 30 s, (b) 40 s, (c) 50 s, (d) 60 s, (e) 70 s and (f) 80 s. The red triangles represent locations of the seismic stations. (For interpretation of the references to color in this figure legend, the reader is referred to the web version of this article.)
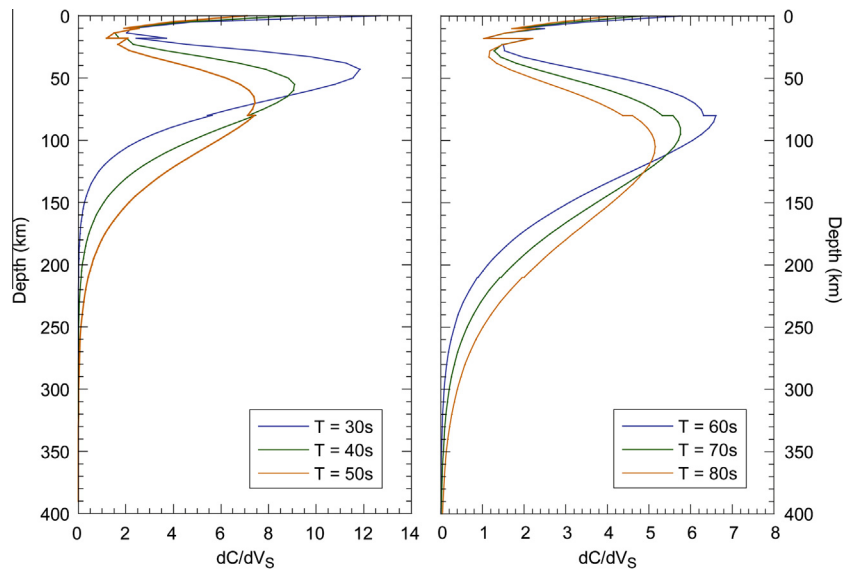
Fig. 9. Sensitivities of the Rayleigh-wave phase velocities to shear-wave speed as functions of depth for selected periods.

We then investigated the effect of regularization parameters. Here, we discuss the influence of norm damping and smoothing on the properties of the resulting model. Resolution is mainly controlled by the cumulative sensitivity of the available data to isotropic and anisotropic perturbations of the medium, but also by additional *a priori* constraints such as norm damping and smooth-

ing. The norm damping is used to constrain the amplitudes of phase-velocity perturbations during the inversion. Therefore, investigating the influence of this parameter allows us to calibrate our inversion. As shown in Fig. 11(e)–(h), the isotropic damping does not affect the lateral distribution of the anomalies or the anisotropic part. Increasing norm damping decreases the amplitude of
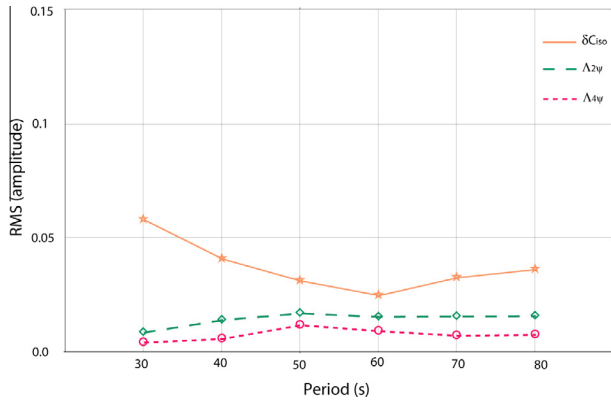
Fig. 10. RMS of the amplitudes calculated for all periods for the isotropic terms (orange), the 2Ψ anisotropy (green) and the 4Ψ term (red). (For interpretation of the references to color in this figure legend, the reader is referred to the web version of this article.)

the velocity anomaly. Therefore the parameter has been set to ensure a good agreement between the resulting model and the initial dispersion curves, from which the average velocity at selected periods is known and the amplitudes of velocity perturbations can be estimated. Similar tests have been performed to estimate the amount of damping necessary for the anisotropic part of the model (Fig. 11(i)–(l)).

Lateral smoothing penalizes the difference between the anomaly at a model knot and the average of the anomalies at its neighboring knots by minimizing the first and second spatial derivatives of velocity anomalies. The lateral smoothing weight is set up independently for each period. We apply a stronger smoothing with decreasing path coverage. Fig. 11(m)–(p) shows the effect of smoothing on the resulting velocity model at a specific period of 40 s. If the smoothing weight is too low (Fig. 11m), small-scale artifacts may appear in the regions with poor data coverage (i.e. at the borders of the model). If the smoothing weight is instead too high, information on small-scale features is lost (Fig. 11p). Therefore, we imposed a smoothing weight large enough in order to avoid artifacts yet still allowing the resolution of regional and local anomalies. Fig. 11(m)–(p) further shows that the anisotropic pattern remains mostly unchanged, indicating the robustness of the inversion.

Similar tests have been conducted for the smoothing of the anisotropic parameters (Fig. 11(q)–(t)). During all those tests on isotropic and anisotropic smoothing and damping, we selected all parameters independently. The resulting smoothness of isotropic, 2ψ and 4ψ anisotropies are checked carefully, to ensure there is limited leaking from anisotropy to isotropic. The resulting L-curves are displayed Fig. 12. This figure highlight the fact that there is a low trade-off between the isotropic and anisotropic terms during the inversion process, which is already suggested by the resolution tests on smoothing and damping parameters.

When the anisotropic smoothing factor increases, information on the local changes of fast direction of the anisotropy vanishes, and only the average direction of the anisotropy in the region (for a selected period) is visible. We then test the robustness of the structures imaged by our inversion, by performing a series of resolution tests (Fig. 13). For each test, an input test model is first created with representative patterns for both isotropic and anisotropic anomalies (Fig. 13(a)–(c)). We then generate synthetic data from these input models, and invert these synthetic data under the same conditions as the real data (Fig. 13(d)–(f)). In particular, the same amount of smoothing and damping, and the same path coverage are used for a given period. This allows testing for the

reconstruction of both isotropic anomalies and anisotropic patterns. The retrieval of the isotropic anomalies should display correct amplitudes and locations. The anisotropic features should be retrieved with consistent directions and amplitudes. Note that the resolution tests presented here addressed the coverage by the data only and no additional noise has been added. The main sources of errors in the actual inversions are those in the dispersion curves and diffraction effects, which are not accounted for by the approximate sensitivity kernels $K_i(\varphi, \theta)$ in Eq. (3) that we used. Given the very substantial redundancy of our coverage provided by the hundreds of crossing paths, random errors are unlikely to have any systematic impact on the results (Legendre et al., 2012). Inversion result shows only small deviation between input and output models both in the azimuth of fast direction and in amplitude. In addition, the output model did not show substantial isotropic perturbations.

Finally, to test the ability of the anisotropy to explain the raw data, we performed a set of inversions in which anisotropic terms are neglected. Damping and smoothing are similar to those of the preferred model. Because the number of parameters is not the same among the inversions, comparing the variance reductions obtained for each inversion is meaningless. Therefore, we computed the reduced χ^2, as defined by Trampert and Woodhouse (2003):

$$\chi^2 = \frac{1}{N_P - T_r}(d - Gm)^T C_d^{-1}(d - Gm) \qquad (4)$$

where N_P is the number of data, T_r the trace of the resolution matrix, d the data, G the kernel matrix, m the model vector, and C_d the covariance matrix. Models with smaller reduced χ^2 explain the data better. To decide whether differences in reduced χ^2 are significant, we performed F-tests (Bevington and Robinson, 2003). For all periods, the reduced χ^2 is smaller when anisotropy is accounted for (Fig. 14). However, the decrease in χ^2 is modest in the period ranges 30–70 s, and F-tests show that these differences are not significant. At periods of 80 s, the decrease in χ^2 is more relevant, and F-tests indicate that it is slightly more significant. The reduced χ^2 decreases further when 4ψ terms are accounted for, but compared to the model with isotropic and 2ψ terms only, differences are very small and F-tests show that this χ^2 reduction is not significant. Overall, these tests suggest that the contribution of the 2ψ anisotropic term and the 4ψ anisotropic term may not be needed to explain our data in all our period ranges, which is consistent with previous study by Abe and Kanamori (1970). However, because the amplitudes of the 2ψ and 4ψ anisotropy are not negligible compared to the isotropic anomalies, we accounted for these terms in the inversion. Furthermore, we propose a possible interpretation for the 2ψ anisotropy (Sections 4 and 5) that is consistent with the identified tectonic and geodynamics events, thus giving support to the presence of anisotropy.

4. Results

Fig. 15 plots our preferred model for selected periods in the range 30–80 s. The background color map represents the isotropic anomalies, and the direction and size of the bars indicate the direction of fast propagation and amplitude of 2ψ anisotropy.

At periods of 30 s and 40 s (Fig. 15 a and b), the pattern of isotropic anomalies is dominated by two main regions. The central part of the Sea of Japan mostly displays fast velocities (up to +5% velocity perturbations), whereas the surrounding regions show slow velocities (up to −4% perturbations in the east). Interestingly, at 40 and 50 s, the separation between slow and fast velocities is well correlated with the boundary between the Okhotsk and Amur plates (Bird, 2003). Around 60 s period, there is a change in the
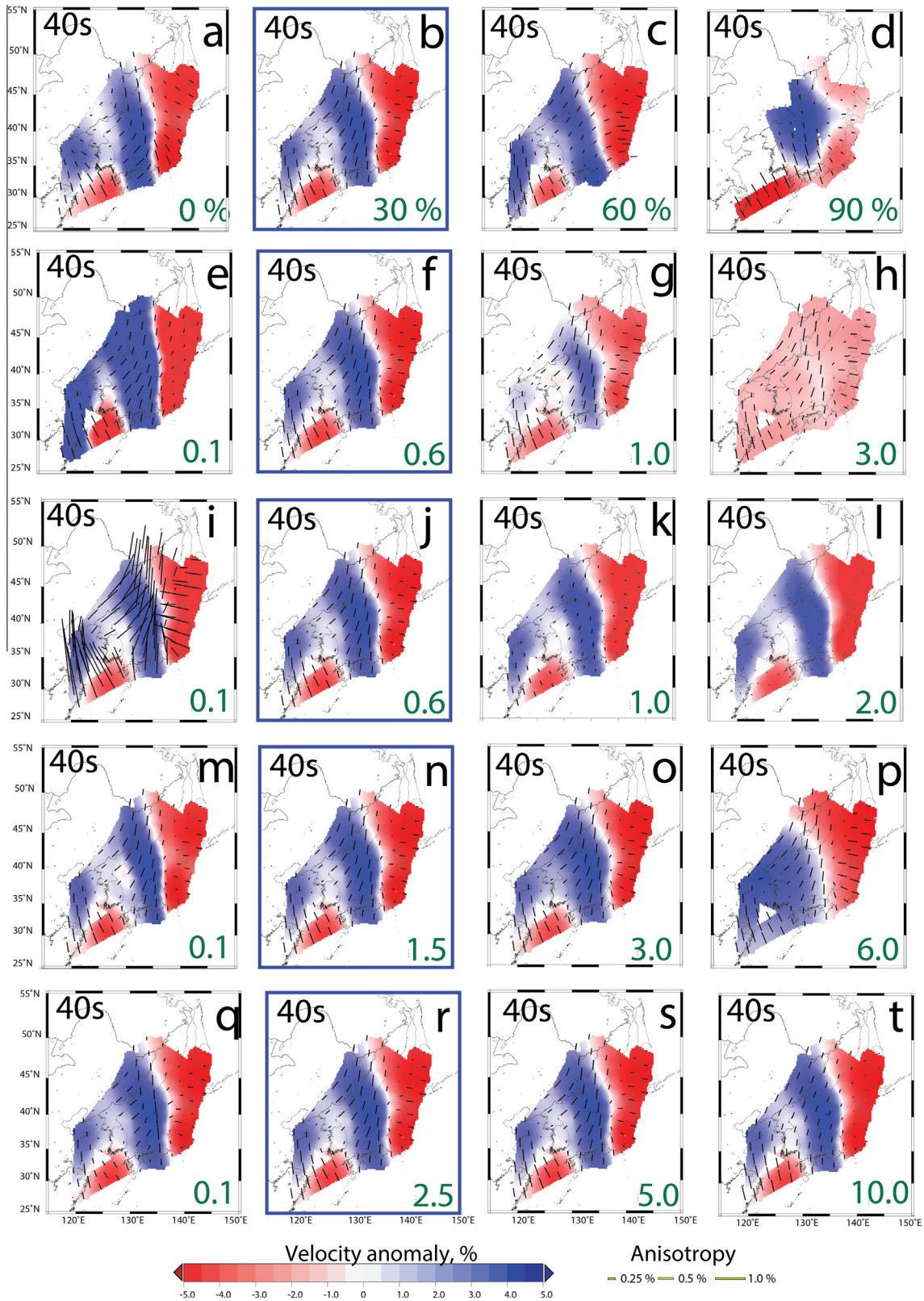
Fig. 11. Inversion tests. The models have been calculated for a specific period of 40 s with our preferred parameters (framed in dark blue in panels b, f, j, n and r), with decreasing percentage in the rejection of data, from (a) 0% to (d) 90% with an interval of 30% between each image, increasing damping values from (e) to (h) for isotropic components, increasing damping values from (i) to (l) for anisotropic components, increasing smoothing values from (m) to (p) for isotropic components, and increasing smoothing values from (q) to (t) for anisotropic components. The preferred parameter chosen for the final inversion is framed in dark blue. The number in green in the bottom right indicates the chosen value for the selected parameter. (For interpretation of the references to color in this figure legend, the reader is referred to the web version of this article.)
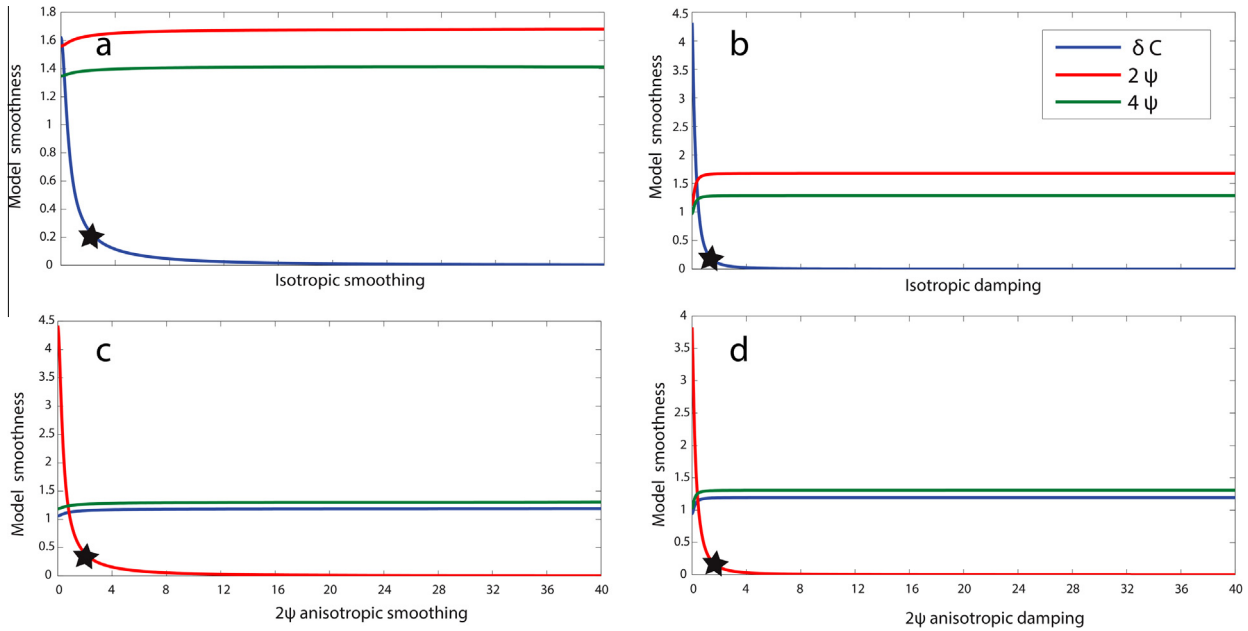
Fig. 12. Smoothness of the models calculated with respect to the selected parameters for the smoothing on the isotropic component (a), the damping on the isotropic component (b), the smoothing on the anisotropic component (c), and the damping on the anisotropic component (d). The blue curves are the model smoothness for the isotropic part of the model, the red curves are the model smoothness for the 2ψ anisotropy part of the model, and the green curves are the model smoothness for the 4ψ anisotropy part of the model. The black stars indicate the preferred chosen values for each parameter. (For interpretation of the references to color in this figure legend, the reader is referred to the web version of this article.)
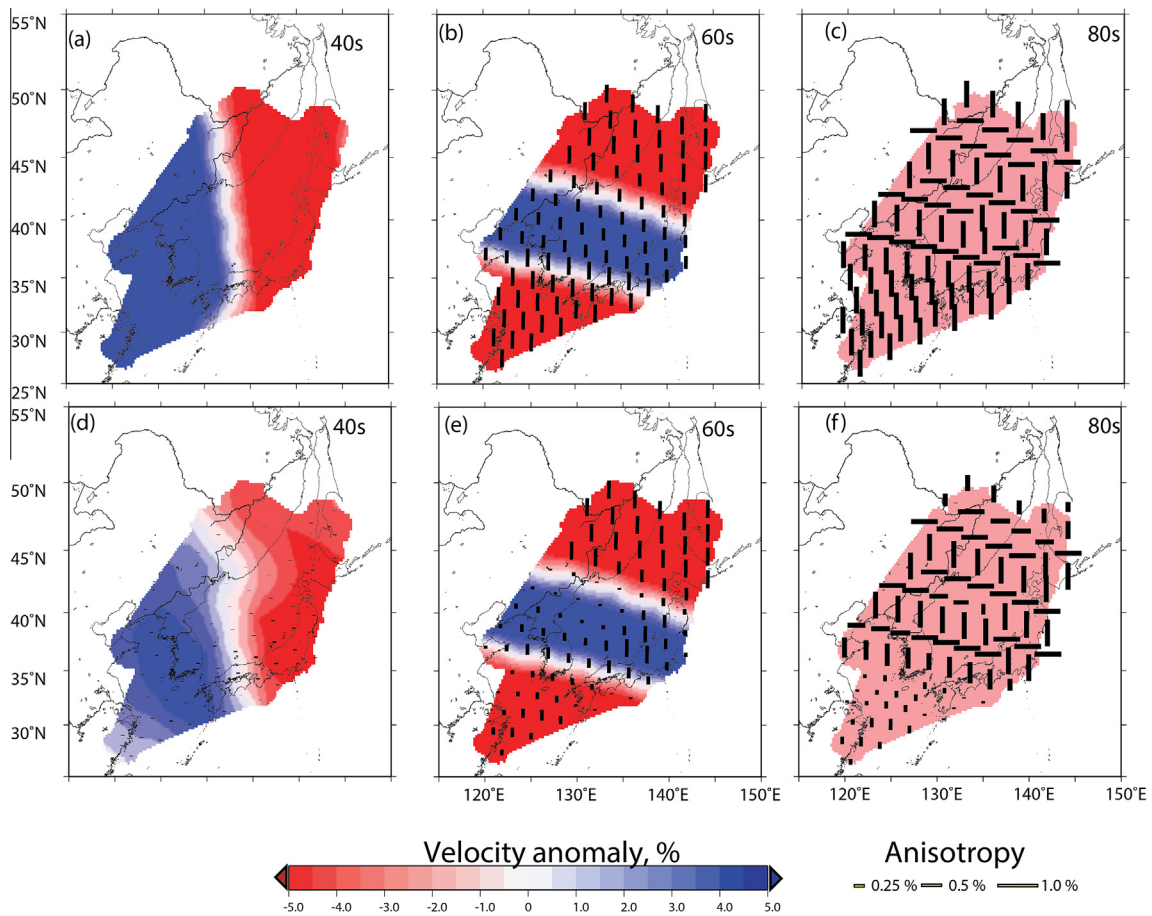
Fig. 13. Resolution tests. (a–c) Input test models at periods of 40, 60 and 80 s; and (d–f) reconstructed models for respective periods. The reconstructions are performed to test the retrieval of both isotropic and anisotropic structures.
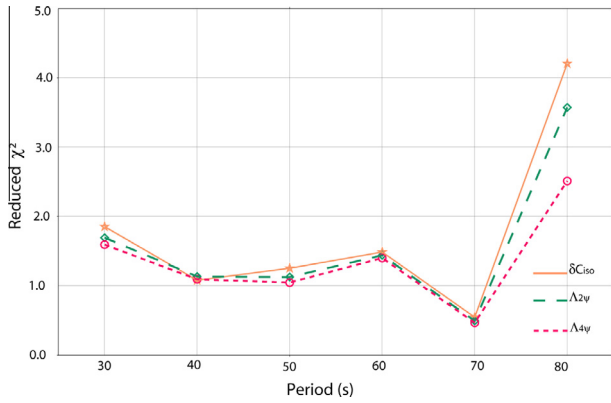
Fig. 14. Reduced χ^2 as a function of period. Inversions are performed for isotropic anomalies only (orange stars), isotropic and 2ψ-anisotropy anomaly (green diamonds), and isotropic and full anisotropy (2ψ and 4ψ) (red circles). The other parameters (grid spacing, rejection, damping and smoothing factors) are the same as those of the preferred values. (For interpretation of the references to color in this figure legend, the reader is referred to the web version of this article.)

northeastern part (up to +5% velocity perturbations) becomes the dominant feature.
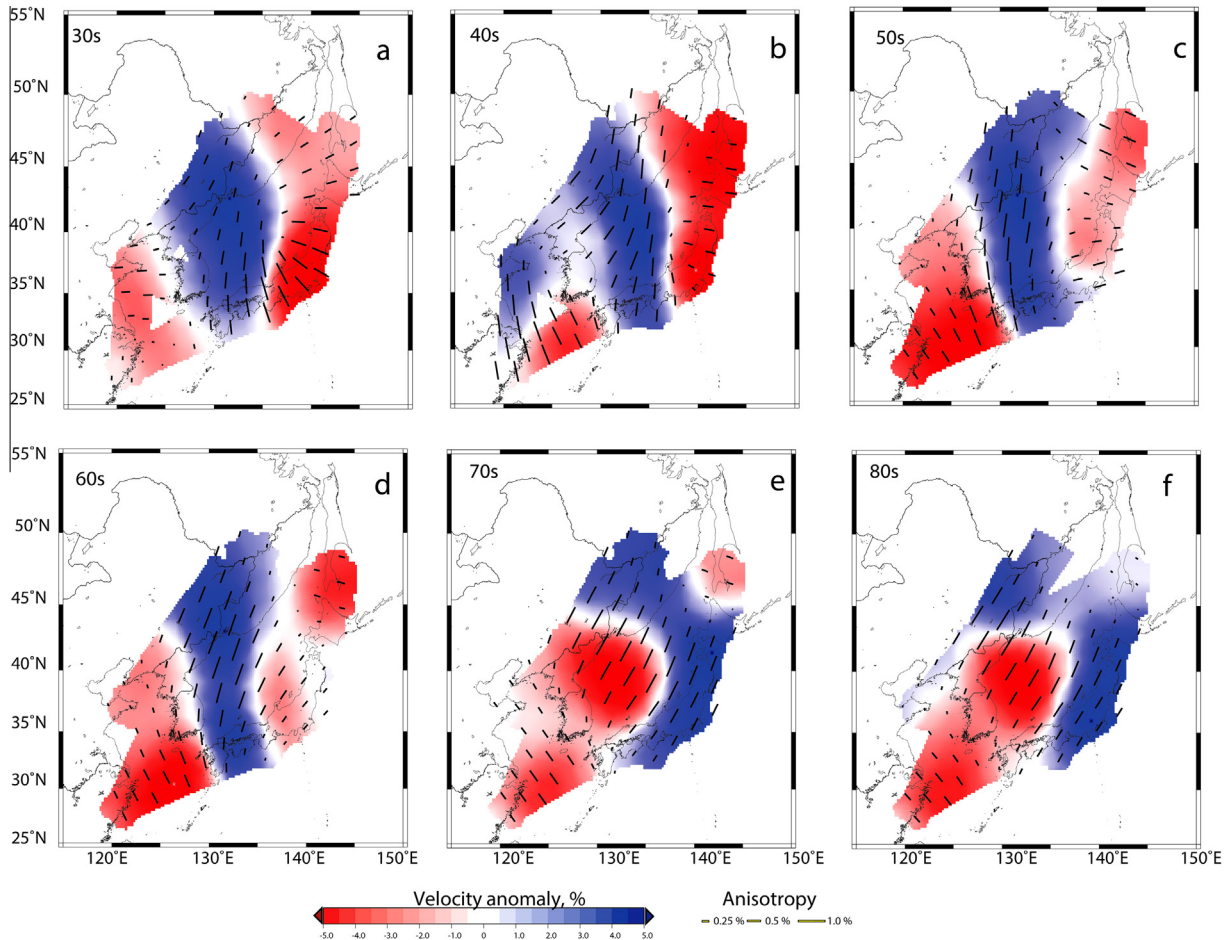
The anisotropic pattern changes with period, but is regionally more coherent than the isotropic pattern. At periods of 40 and 50 s, sampling the lower crust and upper lithospheric mantle, the anisotropy in the Sea of Japan is about 1% in amplitude, with a mostly NE-SW direction of fast propagation. Note that this direction slightly varies around the central part. Furthermore, it turns to a NW-SE direction beneath the Honshu and Hokkaido Islands.

At periods of 60 s and longer, anisotropy is different from that at shorter period. Beneath the Sea of Japan and the Japanese Islands, the 2ψ anisotropy reaches 0.5–1% in amplitude, with a NE-SW direction of fast propagation, i.e. roughly perpendicular to that at 30–40 s. Beneath south of Korea and east of Kyushu, by contrast, the direction of fast propagation is NW-SE.

At periods of 50–70 s, the isotropic and anisotropic patterns change slightly beneath the Sea of Japan (isotropic) and the Japanese Islands (anisotropic). This suggests a transition zone between the anisotropy found at shorter periods (around 30 s) and those found at longer periods (70 s and longer).

5. Discussion

In this section, we discuss our results (Fig. 15) and compare them with previous studies. We also provide some tectonic and geodynamical interpretations for the evolution of the lithosphere beneath the Sea of Japan.

pattern. Fast velocities are found mostly to the northern and eastern part of our model, whereas the central part of the Sea of Japan displays slow velocities (up to −5%). Finally, at 70 and 80 s period, the dominant feature is a dichotomy between the southwestern part of the Sea of Japan (up to −4% perturbations) and its

Fig. 15. Isotropic (background color) and azimuthally anisotropic (yellow lines) phase-velocity maps for specific periods: (a) 30 s, (b) 40 s, (c) 50 s, (d) 60 s, (e) 70 s and (f) 80 s. (For interpretation of the references to color in this figure legend, the reader is referred to the web version of this article.)

5.1. Korean Peninsula

Beneath the Korean Peninsula, our model predicts positive isotropic velocity anomalies in the period range 30–40 s, but negative anomalies at longer periods (50–80 s).

Shorter periods (30 s, sampling the deep crust) display fast velocities beneath Korea, consistent with previous surface-wave tomographic imaging by Cho et al. (2007) and ambient noise cross-correlation study by Kang and Shin (2006). At 30–40 s, the fast velocities are also in good agreement with tomographic studies at larger scale (Friederich, 2003; Lebedev and Nolet, 2003; Gao et al., 2011; Legendre et al., 2015b), and are consistent with previous observations and crustal models of mainland China (Zheng et al., 2008; Sun et al., 2010; Zhou et al., 2012), receiver function analyses (Yoo et al., 2007; Chen et al., 2010), gravity measurements (Xu, 2007), and surface-wave analysis of the East China Sea and Korean Peninsula (Legendre et al., 2014b). Our phase-velocity maps beneath the Korean Peninsula are furthermore in agreement with previous studies and with characteristic features of the geological map of the region, displaying high velocities in the regions where granitoid basement rock outcrops are located (Pouclet et al., 1994; Kang and Shin, 2006; Cho et al., 2007; Yoo et al., 2007; Choi et al., 2013; Lee et al., 2015).

The anisotropic pattern is fairly stable in the lithosphere beneath the Korean Peninsula (sampled by periods of 50 s and larger), displaying very small amplitudes. This coincides well with the timing of the volcanic activity during the Mesozoic and Cenozoic (Kim et al., 2014). The lack of recent volcanic activity, combined with the fast velocities found at periods of 30 and 40 s, suggests the presence of a possible deep magmatic reservoir, inferred by slow velocities found at 50 s and longer, as already observed in Legendre et al. (2014b).

5.2. Japan Basin

In the northern part of our model, covering the Japan Basin (Fig. 1), the path coverage is quite sparse (Fig. 8) due to the lack of seismic stations deployed in the north (Fig. 2). In this region, our models display slow velocities beneath the Japan Basin in the period range 30–50 s, and fast velocities for periods of 70 s and longer. This correlates well with the variations of thickness of the crust, i.e. thicker in the south and thinner beneath the Japan Basin (Kim et al., 1994; Kurashimo et al., 1996; Sato et al., 2004): thick crust will display lower velocities in the shallow lithospheric depth because surface waves sensitive to that depth wave will sample more crustal than lithospheric mantle due to the thick crust. The decrease in crustal thickness towards the north was widely influenced by the tectonic history of the back-arc spreading that formed the Sea of Japan from 32 to 10 Ma (Tamaki, 1992; Pouclet et al., 1994; Choi et al., 2013; Zahirovic et al., 2013, 2014; Yoon et al., 2014).

At periods of 30–40 s, the direction of fast propagation in the Japan Basin is mostly NE-SW, parallel to the direction of the opening of the Sea of Japan. This area belongs to the North American Plate or Okhotsk Plate, which displays slow velocities beneath the Japanese Islands and beneath the Japan Basin at periods of 30–60 s, and fast velocities at periods of 70 s and longer. For periods longer than 60 s, sampling the top of the asthenosphere, the anisotropy beneath the central part of the Sea of Japan is parallel to the direction of the Absolute Plate Motion (DeMets et al., 1990, 1994; Bird, 2003) of the Amur Plate (roughly NNE/SSW), as shown in Fig. 1, suggesting that it results from current deformation related to asthenospheric flow. At shorter periods (40–50 s), sampling the lower crust, the direction of fast propagation is again NE-SW, but the possible origin of the anisotropy is less clear. The fast direction does not fit the direction of the opening of the Sea

of Japan. Because it matches the APM of the Amur Plate (Bird, 2003), it could be related to an earlier motion of the Amur Plate, as the lithosphere was thinner.

5.3. Subduction zones

Beneath the Japanese Islands, slow velocities are found at periods in the range 30–60 s, whereas fast velocities are seen at longer periods (70–80 s). Beneath the Japanese Islands, the slabs are dipping at an angle of about 30° (Hasegawa et al., 2013; Liu et al., 2013), and the slow velocity observed at 30–60 s in this region may be related to crustal thickening above the slab (Fig. 16). Rayleigh waves at these periods would then sample the crust beneath the Japanese Islands, and the lithospheric mantle west of these islands. It is also interesting to note that the transition between the fast and slow velocity is well correlated with the boundary between the Okhotsk and Amur plates (Bird, 2003). The orientation of the fast axis of anisotropy is also very different from the surrounding areas, indicating a different mechanism of deformation. Beneath the subduction zone, trench-normal anisotropy can be seen at periods of 30–40 s, whereas a trench-parallel anisotropy is found at longer periods (70–80 s).

The trench perpendicular anisotropy at periods of 30–60 s could be related to crustal slicing triggered by the descent of the slab. Such a mechanism was suggested to explain seismic anisotropy observed in the central Alps (Fry et al., 2010). Trench-parallel anisotropy, as we observe here in the range 70–80 s, has not been observed in all subduction system, but Long and van der Hilst (2006) concluded that for the Ryukyu subduction system the most likely explanation for the observations of trench parallel anisotropy is the corner flow in the mantle wedge combined with the B-type olivine fabric (Kao et al., 1998; Kneller et al., 2005). Anisotropy beneath the Japan subduction zone has been investigated using SKS splitting measurements (Nakajima and Hasegawa, 2004; Tono et al., 2009; Huang et al., 2011), and P-wave azimuthal anisotropy (Ishise and Oda, 2005; Wei et al., 2015; Zhao et al., 2015). Most of these studies found a consistent anisotropic pattern beneath the Sea of Japan, with fast direction of the azimuthal anisotropy parallel to the trench in the lithosphere, and trench-normal in the asthenosphere. Behn et al. (2007) considered several models to explain the trench-parallel anisotropy under the volcanic front, including slab rollback, oblique subduction, and deformation of water-rich olivine, to explain trench-parallel anisotropy,
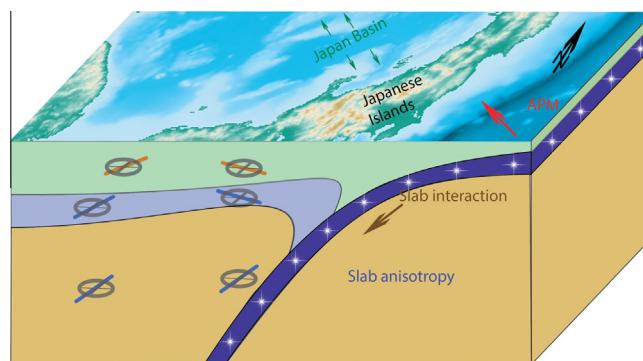
Fig. 16. Sketch of the possible deformation pattern in the region based on our anisotropic model. The average anisotropic patterns at different periods (orange: 30 s, sampling the upper lithosphere; blue: 60 s, sampling the lower lithospheric and asthenospheric mantle). The origin of the anisotropy is indicated by the green arrows (opening of the Japan Basin) and the brown arrow (slab interaction). The Absolute Plate Motion (Bird, 2003) is indicated with the red arrow. (For interpretation of the references to color in this figure legend, the reader is referred to the web version of this article.)

and concluded that none of these mechanisms are consistent with all observations. Instead, small-scale convection driven by the foundering of dense arc lower crust may explain for the trench-parallel anisotropy, even in settings with orthogonal convergence and no slab rollback.

Although seismic anisotropy in the upper mantle is generally attributed to the crystallographic-preferred orientation (CPO) of olivine crystals, the strong trench-parallel anisotropy observed in several subduction systems (as the Ryukyu Trench) is difficult to explain in terms of olivine anisotropy only. Katayama et al. (2009) showed that the lattice-preferred orientations (LPO) of serpentine, the main hydrous mineral in the upper mantle, can produce the strong trench-parallel seismic anisotropy observed in subduction systems because the anisotropic amplitude due to serpentine is much larger than that due to olivine. Recent shear-wave splitting measurements display constant NW fast direction in a broad region below the mantle wedge of the Japan subduction zone (Tono et al., 2009). The constant NNW fast direction of the anisotropy would be consistent with the anisotropic pattern we observe in this region at periods of 30–40 s (sampling the mantle wedge). These measurements have been attributed to the fossil sea-floor spreading anisotropy in the subducting Pacific slab, due to the fact that such anisotropy may have been preserved during its subduction down to the transition zone (Tono et al., 2009).

5.4. Southern part of the Sea of Japan and East China Sea

In the southern part of our model, south of the Kyushu Island and the Korean Peninsula (Fig. 1), we see fast velocities at shorter periods (30 s) and slow velocities at longer periods (40–80 s). The anisotropy is relatively uniform in this area, with a NW–SE direction at all periods. The low anisotropy at 30 s and the constant direction of the anisotropy at periods of 40 s and longer could indicate that this region has been less affected by surface deformation, with less rifting and no oceanization, leading to a more uniform pattern of anisotropy. The region beneath the Kyushu Island extending towards the Korean Peninsula might be the southern extent of the fast anomaly beneath the continental crust of the Sea of Japan (Ulleung and Yamato Basins). In the east, slow velocities are seen at periods of 30–60 s, probably due to the oceanization of the Japan Basin, whereas in the west, fast velocities are found at similar periods.

5.5. Comparison with previous studies

Our model is generally in good agreement with tomographic studies at larger scale (Friederich, 2003; Lebedev and Nolet, 2003; Gao et al., 2011; Legendre et al., 2015b). However the lack of resolution of those models does not allow for local interpretations. Recent noise tomography for monitoring the Sea of Japan (Yoshizawa et al., 2010; Lee et al., 2015) presents high-resolution tomographic images of the region for shorter periods (up to 30–40 s). These studies focus on the strait between Korea and Japan, and interestingly, we observe similar pattern to those in the isotropic part of our model in this region. Body-wave tomography (Hirahara and Mikumo, 1980; Hirata et al., 1989; Zhu et al., 2002; Honda and Nakanishi, 2003; Matsubara et al., 2005, 2008; Hirose et al., 2008; Zheng et al., 2011) and surface wave tomography (Friederich, 2003; Huang et al., 2003; Lebedev and Nolet, 2003; Legendre et al., 2015b) at a local scale also display similar features to our model, including the dichotomy between the continental and oceanic crust beneath the Sea of Japan.

The main contribution of this work is to present isotropic and azimuthally anisotropic Rayleigh-wave phase-velocity maps beneath the Sea of Japan. Those maps allow the examination of azimuthal anisotropy at different periods (depths), which can be related to the evolution of the lithosphere in this region.

6. Conclusions

We have constructed isotropic and azimuthally anisotropic Rayleigh-wave phase-velocity maps for the Sea of Japan in the period range 30–80 s, and using regional broadband records from multiple networks including the China National Seismic Network, the Korea Meteorological Administration, the National Research Institute for Earth Science and Disaster Prevention in Japan, and the Incorporated Research Institutions for Seismology. This study displays for the first time the examination of azimuthal anisotropy with depth beneath the Sea of Japan, which is summarized in Fig. 16. The models we obtain reveal features changing both laterally and with period (i.e. with depth). Anisotropy is not needed to explain the raw data. However, if it is present, our models resolve two distinct anisotropic layers, which may have different origins. In the period range 30–50 s, anisotropy beneath the Japanese Islands may be related to crustal slicing. The origin of the anisotropy we observe at these periods in the Sea of Japan is more uncertain. At periods of 60 s and longer, sampling the top of the asthenosphere, anisotropy may be related to asthenospheric flow. The anisotropic pattern coupled with the isotropic velocity perturbations can be used to sketch the tectonic units in the region: the boundary between continental and oceanic lithospheres, and the boundary between North American, Eurasian and Pacific plates.

References

Abe, K., Kanamori, H., 1970. Upper mantle structure of the Philippine Sea. Island Arc Ocean 54, 85–91.

Abe, K., Kanamori, H., 1971. Mantle structure beneath the Japan Sea as revealed by surface waves. Bull. Earthquake Res. Inst. 48, 1011–1021.

Aki, K., 1968. Seismological evidences for the existence of soft thin layers in the upper mantle under Japan. J. Geophys. Res. 73, 585–594.

Aki, K., Kaminuma, K., 1963. Phase velocity of low waves in Japan (part 1): love waves from the Aleutian shock of March 9, 1957. Bull. Earthquake Res. Inst. 41, 243–259.

Asamori, K., Zhao, D., 2015. Teleseismic shear wave tomography of the Japan subduction zone. Geophys. J. Int. 203 (3), 1752–1772.

Behn, M.D., Hirth, G., Kelemen, P.B., 2007. Trench-parallel anisotropy produced by foundering of arc lower crust. Science 317, 108–111.

Bevington, P., Robinson, D., 2003. Data Reduction and Error Analysis for the Physical Sciences. McGraw-Hill Higher Education, McGraw-Hill.

Bird, P., 2003. An updated digital model of plate boundaries. Geochem. Geophys. Geosyst. 4, 1–52.

Bourova, E., Yoshizawa, K., Yomogida, K., 2010. Upper mantle structure of marginal seas and subduction zones in northeastern Eurasia from Rayleigh wave tomography. Phys. Earth Planet. Inter. 183, 20–32.

Chen, Y., Niu, F., Liu, R., Huang, Z., Tkalčić, H., Sun, L., Chan, W., 2010. Crustal structure beneath China from receiver function analysis. J. Geophys. Res.: Solid Earth 115, B03307.

Cho, K., Herrmann, R., Ammon, C., Lee, K., 2007. Imaging the upper crust of the Korean Peninsula by surface-wave tomography. Bull. Seismol. Soc. Am. 97, 198–207.

Choi, H., Hong, T.K., He, X., Baag, C.E., 2012. Seismic evidence for reverse activation of a paleo-rifting system in the East Sea (Sea of Japan). Tectonophysics 572, 123–133.

Choi, H.O., Choi, S.H., Lee, D.C., Kang, H.C., 2013. Geochemical evolution of basaltic volcanism within the tertiary basins of southeastern Korea and the opening of the East Sea (Sea of Japan). J. Volcanol. Geoth. Res. 249, 109–122.

DeMets, C., Gordon, R.G., Argus, D., Stein, S., 1990. Current plate motions. Geophys. J. Int. 101, 425–478.

DeMets, C., Gordon, R.G., Argus, D.F., Stein, S., 1994. Effect of recent revisions to the geomagnetic reversal time scale on estimates of current plate motions. Geophys. Res. Lett. 21, 2191–2194. http://dx.doi.org/10.1029/94GL02118.

Deschamps, F., Lebedev, S., Meier, T., Trampert, J., 2008. Azimuthal anisotropy of Rayleigh-wave phase velocities in the east-central United States. Geophys. J. Int. 173, 827–843. http://dx.doi.org/10.1111/j.1365-246X.2008.03751.x.

Endrun, B., Lebedev, S., Meier, T., Tirel, C., Friederich, W., 2011. Complex layered deformation within the Aegean crust and mantle revealed by seismic anisotropy. Nat. Geosci. 4, 203–207.

Evans, J.R., Suyehiro, K., Sacks, I., 1978. Mantle structure beneath the Japan Sea – a re-examination. Geophys. Res. Lett. 5, 487–490.

Friederich, W., 2003. The S-velocity structure of the East Asian mantle from inversion of shear and surface waveforms. Geophys. J. Int. 153, 88–102. http://dx.doi.org/10.1046/j.1365-246X.2003.01869.x.

Fry, B., Deschamps, F., Kissling, Edi., Stehly, L., Giardini, D., 2010. Layered azimuthal anisotropy of Rayleigh wave phase velocities in the European Alpine lithosphere inferred from ambient noise. Earth Planet. Sci. Lett. 291 (1), 89–125.

Fryer, P., 1996. Evolution of the Mariana convergent plate margin system. Rev. Geophys. 34, 95–102. http://dx.doi.org/10.1029/95RG03476.

Gao, Y., Wu, J., Fukao, Y., Shi, Y., Zhu, A., 2011. Shear wave splitting in the crust in north China: stress, faults and tectonic implications. Geophys. J. Int. 187, 642–654.

Hasegawa, A., Nakajima, J., Yanada, T., Uchida, N., Okada, T., Zhao, D., Matsuzawa, T., Umino, N., 2013. Complex slab structure and arc magmatism beneath the Japanese islands. J. Asian Earth Sci. 78, 277–290, Evolving Asia.

He, H., Tsukuda, E., 2003. Recent progresses of active fault research in China. J. Geogr. 112, 489–520.

Hirahara, K., Mikumo, T., 1980. Three-dimensional seismic structure of subducting lithospheric plates under the Japan Islands. Phys. Earth Planet. Inter. 21, 109–119.

Hirata, N., Tokuyama, H., Chung, T.W., 1989. An anomalously thick layering of the crust of the Yamato basin, southeastern Sea of Japan: the final stage of back-arc spreading. Tectonophysics 165, 303–314.

Hirose, F., Nakajima, J., Hasegawa, A., 2008. Three-dimensional seismic velocity structure and configuration of the Philippine Sea slab in southwestern Japan estimated by double-difference tomography. J. Geophys. Res.: Solid Earth 113, B09315.

Honda, S., Nakanishi, I., 2003. Seismic tomography of the uppermost mantle beneath southwestern Japan: seismological constraints on modelling subduction and magmatism for the Philippine Sea slab. Earth Planets Space 55, 443–462.

Huang, J., Zhao, D., 2006. High-resolution mantle tomography of China and surrounding regions. J. Geophys. Res.: Solid Earth 111, B09305.

Huang, Z., Zhao, D., Wang, L., 2011. Shear wave anisotropy in the crust, mantle wedge, and subducting Pacific slab under northeast Japan. Geochem. Geophys. Geosyst. 12.

Huang, Z., Li, H., Zheng, Y., Peng, Y., 2009. The lithosphere of North China Craton from surface wave tomography. Earth Planet. Sci. Lett. 288, 164–173.

Huang, Z., Su, W., Peng, Y., Zheng, Y., Li, H., 2003. Rayleigh wave tomography of China and adjacent regions. J. Geophys. Res.: Solid Earth 108, 2073.

Ishise, M., Oda, H., 2005. Three-Dimensional structure of P-wave anisotropy beneath the Tohoku district, northeast Japan. J. Geophys. Res.: Solid Earth 110, 16.

Kang, T.S., Shin, J.S., 2006. Surface-wave tomography from ambient seismic noise of accelerograph networks in southern Korea. Geophys. Res. Lett. 33, L17303.

Kao, H., Shen, S.S.J., Ma, K.F., 1998. Transition from oblique subduction to collision: earthquakes in the southernmost Ryukyu Arc-Taiwan region. J. Geophys. Res.: Solid Earth 103, 7211–7229.

Katayama, I., Hirauchi, K.I., Michibayashi, K., Ando, J.I., 2009. Trench-parallel anisotropy produced by serpentine deformation in the hydrated mantle wedge. Nature 461, 1114–1117.

Kennett, B.L.N., Engdahl, E.R., Buland, R., 1995. Constraints on seismic velocities in the Earth from traveltimes. Geophys. J. Int. 122, 108–124.

Kim, H.J., Park, C.H., Hong, J.K., Jou, H.T., Chung, T.W., Zhigulef, V., Anosov, G., 1994. A seismic experiment in the Ulleung basin (Tsushima basin), southwestern Japan Sea (East Sea of Korea). Geophys. Res. Lett. 21, 1975–1978.

Kim, S.W., Kwon, S., Yi, K., Santosh, M., 2014. Arc magmatism in the Yeongnam massif, Korean Peninsula: imprints of Columbia and Rodinia supercontinents. Gondwana Res. 26, 1009–1027.

Kneller, E.A., van Keken, P.E., ichiro Karato, S., Park, J., 2005. B-type olivine fabric in the mantle wedge: insights from high-resolution non-newtonian subduction zone models. Earth Planet. Sci. Lett. 237, 781–797.

Knopoff, L., 1972. Observation and inversion of surface-wave dispersion. Tectonophysics 13, 497–519.

Kobayashi, K., Isezaki, N., 1976. Magnetic anomalies in the Sea of Japan and the Shikoku Basin: possible tectonic implications. Am. Geophys. Union, 235–251. http://dx.doi.org/10.1029/GM019p0235.

Kurashimo, E., Shinohara, M., Suyehiro, K., Kasahara, J., Hirata, N., 1996. Seismic evidence for stretched continental crust in the Japan Sea. Geophys. Res. Lett. 23, 3067–3070.

Lallemand, S., Jolivet, L., 1986. Japan Sea: a pull-apart basin? Earth Planet. Sci. Lett. 76, 375–389.

Lebedev, S., Meier, T., van der Hilst, R., 2006. Asthenospheric flow and origin of volcanism in the Baikal rift area. Earth Planet. Sci. Lett. 249, 415–424.

Lebedev, S., Nolet, G., 2003. Upper mantle beneath Southeast Asia from S velocity tomography. J. Geophys. Res.: Solid Earth 108, 2048. http://dx.doi.org/10.1029/2000JB000073.

Lebedev, S., Van Der Hilst, R.D., 2008. Global upper-mantle tomography with the automated multimode inversion of surface and S-wave forms. Geophys. J. Int. 173, 505–518.

Lee, S.J., Rhie, J., Kim, S., Kang, T.S., Kim, G., 2015. Ambient seismic noise tomography of the southern East Sea (Japan Sea) and the Korea Strait. Geosci. J., 1–12 http://dx.doi.org/10.1007/s12303-015-0012-7.

Legendre, C., Deschamps, F., Zhao, L., Chen, Q.F., 2015c. Rayleigh-wave dispersion reveals crust-mantle decoupling beneath eastern Tibet. Sci. Rep. (16644), 1–7

Legendre, C., Zhao, L., Chen, Q.F., 2015b. Upper-mantle shear-wave structure under East and Southeast Asia from automated multimode inversion of waveforms. Geophys. J. Int. (203), 707–719.

Legendre, C., Zhao, L., Huang, W.G., Huang, B.S., 2015a. Anisotropic Rayleigh-wave phase velocities beneath northern Vietnam. Earth Planets Space 67, 28. http://dx.doi.org/10.1186/s40623-015-0193-3.

Legendre, C.P., Chen, Q.F., Zhao, L., 2014a. Lithospheric structure beneath the East China Sea revealed by Rayleigh-wave phase velocities. J. Asian Earth Sci. 96, 213–225.

Legendre, C.P., Deschamps, F., Zhao, L., Lebedev, S., Chen, Q.F., 2014b. Anisotropic Rayleigh wave phase velocity maps of eastern China. J. Geophys. Res.: Solid Earth 119, 4802–4820. http://dx.doi.org/10.1002/2013JB010781.

Legendre, C.P., Meier, T., Lebedev, S., Friederich, W., Viereck-Götte, L., 2012. A shear wave velocity model of the European upper mantle from automated inversion of seismic shear and surface waveforms. Geophys. J. Int. 191, 282–304. http://dx.doi.org/10.1111/j.1365-246X.2012.05613.x.

Lei, J., Xie, F., Fan, Q., Santosh, M., 2013. Seismic imaging of the deep structure under the Chinese volcanoes: an overview. Phys. Earth Planet. Inter. 224, 104–123.

Lei, J., Zhao, D., 2005. P-wave tomography and origin of the Changbai intraplate volcano in northeast Asia. Tectonophysics 397, 281–295.

Lei, J., Zhao, D., Xie, F., Liu, J., 2011. An attempt to detect temporal variations of crustal structure in the source area of the 2006 Wen-An earthquake in north China. J. Asian Earth Sci. 40, 958–976.

Liu, X., Zhao, D., 2015. Seismic attenuation tomography of the southwest Japan arc: new insight into subduction dynamics. Geophys. J. Int. 201, 135–156.

Liu, X., Zhao, D., 2016. P and S wave tomography of Japan subduction zone from joint inversions of local and teleseismic travel times and surface-wave data. Phys. Earth Planet. Inter. 252, 1–22.

Liu, X., Zhao, D., Li, S., 2013. Seismic imaging of the southwest Japan arc from the Nankai trough to the Japan Sea. Phys. Earth Planet. Inter. 216, 59–73.

Long, M.D., van der Hilst, R.D., 2006. Shear wave splitting from local events beneath the Ryukyu arc: trench-parallel anisotropy in the mantle wedge. Phys. Earth Planet. Inter. 155, 300–312.

Ludwig, W.J., Murauchi, S., Houtz, R.E., 1975. Sediments and structure of the Japan Sea. Geol. Soc. Am. Bull. 86, 651–664.

Matsubara, M., Hayashi, H., Obara, K., Kasahara, K., 2005. Low-velocity oceanic crust at the top of the Philippine Sea and Pacific plates beneath the Kanto region, central Japan, imaged by seismic tomography. J. Geophys. Res.: Solid Earth 110, B12304.

Matsubara, M., Obara, K., Kasahara, K., 2008. Three-dimensional P-and S-wave velocity structures beneath the Japan islands obtained by high-density seismic stations by seismic tomography. Tectonophysics 454, 86–103.

Meier, T., Dietrich, K., Stöckhert, B., Harjes, H.P., 2004. One-dimensional models of shear wave velocity for the eastern Mediterranean obtained from the inversion of Rayleigh wave phase velocities and tectonic implications. Geophys. J. Int. 156, 45–58. http://dx.doi.org/10.1111/j.1365-246X.2004.02121.x.

Miyashiro, A., 1986. Hot regions and the origin of marginal basins in the western Pacific. Tectonophysics 122, 195–216.

Montagner, J.P., Tanimoto, T., 1990. Global anisotropy in the upper mantle inferred from the regionalization of phase velocities. J. Geophys. Res. 95, 4797–4819.

Montagner, J.P., Tanimoto, T., 1991. Global upper mantle tomography of seismic velocities and anisotropies. J. Geophys. Res. 962, 20337–20351.

Nakajima, J., Hasegawa, A., 2004. Shear-wave polarization anisotropy and subduction-induced flow in the mantle wedge of northeastern Japan. Earth Planet. Sci. Lett. 225, 365–377.

Pouclet, A., Lee, J.S., Vidal, P., Cousens, B., Bellon, H., 1994. Cretaceous to Cenozoic volcanism in South Korea and in the Sea of Japan: magmatic constraints on the opening of the back-arc basin. Geol. Soc. Lond. Spec. Publ. 81, 169–191.

Ren, J., Li, S., 2000. Spreading and dynamic setting of marginal basins of the western Pacific. Earth Sci. Front. 7, 203–213.

Sato, T., Shinohara, M., Karp, B.Y., Kulinich, R.G., Isezaki, N., 2004. P-wave velocity structure in the northern part of the central Japan Basin, Japan Sea with ocean bottom seismometers and airguns. Earth Planets Space 56, 501–510.

Sato, Y., 1955. Analysis of dispersed surface waves by means of Fourier Transform I. Bull. Earthquake Res. Inst. 33, 33–48.

Spindel, R.C., Na, J., Dahl, P.H., Oh, S., Eggen, C., Kim, Y.G., Akulichev, V.A., Morgunov, Y.N., 2003. Acoustic tomography for monitoring the Sea of Japan: a pilot experiment. IEEE J. Oceanic Eng. 28, 297–302.

Sun, X., Song, X., Zheng, S., Yang, Y., Ritzwoller, M., 2010. Three dimensional shear wave velocity structure of the crust and upper mantle beneath China from ambient noise surface wave tomography. Earthquake Sci. 23, 449–463. http://dx.doi.org/10.1007/s11589-010-0744-4.

Takahashi, H., Kasahara, M., Kimata, F., Miura, S., Heki, K., Seno, T., Kato, T., Vasilenko, N., Ivashchenko, A., Bahtiarov, V., 1999. Velocity field of around the Sea of Okhotsk and Sea of Japan regions determined from a new continuous GPS network data. Geophys. Res. Lett. 26, 2533–2536.

Tamaki, K., 1992. Tectonic synthesis and implications of Japan Sea ODP drilling. In: Proc. ODP, Sci. Results.. College Station, pp. 1333–1348.

Tapponnier, P., Molnar, P., 1976. Slip-line field theory and large-scale continental tectonics. Nature 264, 319–324.

Tatsumi, Y., Maruyama, S., Nohda, S., 1990. Mechanism of backarc opening in the Japan Sea: role of asthenospheric injection. Tectonophysics 181, 299–306.

Tobin, H.J., Kinoshita, M., 2006. NanTroSEIZE: the IODP Nankai Trough seismogenic zone experiment. Sci. Drill 2, 23–27.

Tono, Y., Fukao, Y., Kunugi, T., Tsuboi, S., 2009. Seismic anisotropy of the Pacific slab and mantle wedge beneath the Japanese Islands. J. Geophys. Res.: Solid Earth, 114.

Trampert, J., Woodhouse, J.H., 2003. Global anisotropic phase velocity maps for fundamental mode surface waves between 40 and 150 s. Geophys. J. Int. 154, 154–165.

Wang, Z., Dahlen, F.A., 1995. Spherical-spline parameterization of three-dimensional Earth models. Geophys. Res. Lett. 22, 3099–3102. http://dx.doi.org/10.1029/95GL03080.

Wei, W., Zhao, D., Xu, J., Wei, F., Liu, G., 2015. P and S wave tomography and anisotropy in northwest Pacific and east Asia: constraints on stagnant slab and intraplate volcanism. J. Geophys. Res.: Solid Earth 120 (3), 1642–1666.

Wessel, P., Smith, W.H., 1995. New version of the generic mapping tools. Eos Trans. AGU 76, 329.

Wu, J., Suppe, J., Lu, R., Kanda, R., 2016. Philippine Sea and east Asian plate tectonics since 52 Ma constrained by new subducted slab reconstruction methods. J. Geophys. Res.: Solid Earth, 72. http://dx.doi.org/10.1002/2016JB012923.

Xu, Y.G., 2007. Diachronous lithospheric thinning of the North China Craton and formation of the Daxin'anling-Taihangshan gravity lineament. Lithos 96, 281–298. http://dx.doi.org/10.1016/j.lithos.2006.09.013.

Yin, A., 2010. Cenozoic tectonic evolution of Asia: a preliminary synthesis. Tectonophysics 488, 293–325. http://dx.doi.org/10.1016/j.tecto.2009.06.002.

Yoo, H., Herrmann, R., Cho, K., Lee, K., 2007. Imaging the three-dimensional crust of the Korean Peninsula by joint inversion of surface-wave dispersion and teleseismic receiver functions. Bull. Seismol. Soc. Am. 97, 1002–1011.

Yoon, S., Sohn, Y., Chough, S., 2014. Tectonic, sedimentary, and volcanic evolution of a back-arc basin in the East Sea (Sea of Japan). Mar. Geol. 352, 70–88.

Yoshizawa, K., Miyake, K., Yomogida, K., 2010. 3D upper mantle structure beneath Japan and its surrounding region from inter-station dispersion measurements of surface waves. Phys. Earth Planet. Inter. 183, 4–19.

Zahirovic, S., Seton, M., Müller, R.D., 2013. The Cretaceous and Cenozoic tectonic evolution of Southeast Asia. Solid Earth Discuss. 5, 1335–1422. http://dx.doi.org/10.5194/sed-5-1335-2013.

Zahirovic, S., Seton, M., Müller, R.D., 2014. The Cretaceous and Cenozoic tectonic evolution of Southeast Asia. Solid Earth 5, 227–273. http://dx.doi.org/10.5194/se-5-227-2014.

Zhao, D., Wang, Z., Umino, N., Hasegawa, A., 2009. Mapping the mantle wedge and interplate thrust zone of the northeast Japan Arc. Tectonophysics 467, 89–106.

Zhao, D., Wei, W., Nishizono, Y., Inakura, H., 2011a. Low-frequency earthquakes and tomography in western Japan: insight into fluid and magmatic activity. J. Asian Earth Sci. 42, 1381–1393.

Zhao, D., Yu, S., Liu, X., 2015. Seismic anisotropy tomography: new insight into subduction dynamics. Gondwana Res. http://dx.doi.org/10.1016/j.gr.2015.05.008.

Zhao, D., Yu, S., Ohtani, E., 2011b. East Asia: seismotectonics, magmatism and mantle dynamics. J. Asian Earth Sci. 40, 689–709.

Zheng, S., Sun, X., Song, X., Yang, Y., Ritzwoller, M.H., 2008. Surface wave tomography of China from ambient seismic noise correlation. Geochem. Geophys. Geosyst. 9, 5020. http://dx.doi.org/10.1029/2008GC001981.

Zheng, Y., Yao, Z.X., Liang, J.H., Zheng, J., 2010. The role played and opportunities provided by IGP DMC of China National Seismic Network in Wenchuan earthquake disaster relief and researches. Bull. Seismol. Soc. Am. 100, 2866–2872.

Zheng, Y., Shen, W., Zhou, L., Yang, Y., Xie, Z., Ritzwoller, M.H., 2011. Crust and uppermost mantle beneath the North China Craton, northeastern China, and the Sea of Japan from ambient noise tomography. J. Geophys. Res.: Solid Earth 116, B12312.

Zhou, L., Xie, J., Shen, W., Zheng, Y., Yang, Y., Shi, H., Ritzwoller, M.H., 2012. The structure of the crust and uppermost mantle beneath south China from ambient noise and earthquake tomography. Geophys. J. Int. 189, 1565–1583. http://dx.doi.org/10.1111/j.1365-246X.2012.05423.x.

Zhu, J.S., Cao, J.M., Cai, X.L., Yan, Z.Q., Cao, X.L., 2002. High resolution surface wave tomography in East Asia and west pacific marginal sea. Chin. J. Geophys. 45, 679–698.